Geochemistry Geophysics Geosystems G3

Article
Volume 11, Number 6
8 June 2010
Q06W06, doi:10.1029/2009GC002889
ISSN: 1525-2027

Published by AGU and the Geochemical Society

Toward an explanation for the present and past locations of the poles

B. Steinberger
Center for Geodynamics, NGU, N-7491 Trondheim, Norway

Section 2.5: Geodynamic Modelling, Helmholtz Centre Potsdam, German Research Centre for Geosciences, Telegrafenberg, D-14473 Potsdam, Germany (bstein@gfz-potsdam.de)

PGP, University of Oslo, N-0316 Oslo, Norway

T. H. Torsvik
Center for Geodynamics, NGU, N-7491 Trondheim, Norway

PGP, University of Oslo, N-0316 Oslo, Norway

School of Geosciences, University of Witwatersrand, Johannesburg, South Africa

[1] Earth's orientation relative to its spin axis is determined by its nonhydrostatic inertia tensor. We show here that the present-day nonhydrostatic inertia tensor can be modeled by combining contributions due to large low shear velocity provinces (LLSVPs) in the lowermost mantle and due to subduction. With the first contribution only, the spin axis would be at ~67°N, 96°E (north Siberia). The distribution of recent subduction, with largest amounts in the northwest Pacific (beneath East Asia) and the southeast Pacific (beneath South America), adds a secondary contribution which moves the spin axis toward the observed poles. We use plate reconstructions to infer subduction and inertia tensor through time, assuming that the LLSVP contribution has remained constant. Motion of the pole toward Greenland since ~50 Ma is attributed to increased subduction beneath East Asia and South America and a decrease beneath North America since then. Motion of the pole toward Siberia before that is attributed to large amounts of subduction beneath North America between ~120 and 50 Ma and decreasing amounts of subduction in East Asia after 60–70 Ma. Greater stability of the spin axis since ~100 Ma can be attributed to a decrease in the amount of subduction in polar latitudes and an increase in equatorial latitudes.

Components: 10,900 words, 11 figures.

Keywords: true polar wander; large low shear velocity provinces; subduction.

Index Terms: 8157 Tectonophysics: Plate motions: past (3040); 8124 Tectonophysics: Earth's interior: composition and state (1212); 1239 Geodesy and Gravity: Earth rotation variations.

Received 5 October 2009; **Revised** 30 March 2010; **Accepted** 3 May 2010; **Published** 8 June 2010.

Steinberger, B., and T. H. Torsvik (2010), Toward an explanation for the present and past locations of the poles, *Geochem. Geophys. Geosyst.*, *11*, Q06W06, doi:10.1029/2009GC002889.

Theme: Plate Reconstructions, Mantle Convection, and Tomography Models: A Complementary Vision of Earth's Interior
Guest Editors: D. Müller, S. Quere, and T. Torsvik

1. Introduction

[2] Why are the Earth's poles where they are now? And what has, in the geologic past, determined their motion, or stability? To address these questions, we have to consider that the Earth's spin axis is always nearly identical to the axis of maximum nonhydrostatic moment of inertia. The inertia tensor can be expressed in terms of the spherical harmonic degree 2 component of the geoid. Therefore, in other words, the Earth orients itself relative to its spin axis such that "excess masses" (corresponding to geoid highs) are placed near the equator and mass deficits (geoid lows) near the poles [*Gold*, 1955; *Goldreich and Toomre*, 1969]. Hence the initially posed question can be rephrased to: What determines the Earth's geoid and its change with time?

[3] The long-wavelength (≥ a few 1000 km) part of the geoid is mainly caused by density heterogeneities in the Earth's mantle. Arguably, two main contributions of the latter are (1) the two large low shear velocity provinces (LLSVPs) in the Earth's lowermost mantle, which are a consistent feature of most tomography models [*Su et al.*, 1994; *Masters et al.*, 2000; *Ritsema and van Heijst*, 2000; *Megnin and Romanowicz*, 2000; *Grand*, 2002; *Panning and Romanowicz*, 2006; *Montelli et al.*, 2006; *Kustowski et al.*, 2008; *Simmons et al.*, 2009], and (2) subducted lithospheric slabs sinking through the mantle [*Grand*, 2002; *Grand et al.*, 1997; *van der Voo et al.*, 1999a, 1999b], after possible stagnation in the transition zone [*Fukao et al.*, 2001; *Li et al.*, 2008]. Similarly, it had been shown that the geoid can be divided up into contributions due to slabs, and related to hot spots [*Richards et al.*, 1988] which are, in turn, related to LLSVPs [*Thorne et al.*, 2004; *Burke et al.*, 2008], and that hence the location of the Earth's spin axis is apparently controlled by a combination of mass anomalies related to hot spots and subducted slabs [*Crough and Jurdy*, 1980]. While the two LLSVPs appear to have existed for 300 Myr [*Zhong et al.*, 2007] and maintained their shape for 200 Myr or longer [*Torsvik et al.*, 2006; *Burke et al.*, 2008], the distribution of subduction zones has changed over geologic times.

[4] The shape of the LLSVPs inferred from recent tomography models [*Masters et al.*, 2000; *Ritsema and van Heijst*, 2000; *Megnin and Romanowicz*, 2000; *Grand*, 2002; *Panning and Romanowicz*, 2006; *Montelli et al.*, 2006; *Kustowski et al.*, 2008; *Simmons et al.*, 2009] shows stunning similarities with the geometry of the residual geoid, where the inferred contributions of recent subduction have been removed [*Hager*, 1984]. Notably, LLSVPs are associated with geoid highs. With a negative degree 2 geoid kernel (section 3) in the lower mantle, the LLSVPs need to be associated with negative mantle density anomalies in order to provide a positive geoid. Geoid kernels indicate the combined effect of a density anomaly itself and the topography at the surface and core-mantle boundary (CMB) induced by the viscous flow which is caused by these density anomalies, and a negative kernel means the topography effect is dominant. *Hager et al.* [1985] were the first to show that with appropriate kernels (i.e., negative in the lower mantle), the long-wavelength geoid predicted from seismic tomography matches the observed geoid remarkably well.

[5] Although accumulating evidence from a variety of fields indicates that the two nearly antipodal LLSVPs in the Earth's lowermost mantle are chemically distinct and heavier than the rest of the mantle [*Masters et al.*, 2000; *Burke et al.*, 2008; *Ishii and Tromp*, 1999; *Ni et al.*, 2002; *Wang and Wen*, 2004; *Garnero et al.*, 2007], they can be, in an integrated sense, associated with negative density anomalies, if there is hotter, buoyantly rising material in the mantle above them, either large-scale upwellings or plumes from their edges. The fact that reconstructed eruption sites of large igneous provinces (LIPs) in the geologic past almost always fall close to their present-day margins is an important indication of their stability since 200 Ma [*Torsvik et al.*, 2006] and possibly longer [*Burke et al.*, 2008]. In the "smean" model [*Becker and Boschi*, 2002], which is an average of three tomography models [*Grand*, 2002; *Masters et al.*, 2000; *Ritsema and van Heijst*, 2000] the −1% velocity contour (in its lowermost layer) is a good approximation to these margins, because reconstructed LIP eruption sites and steep

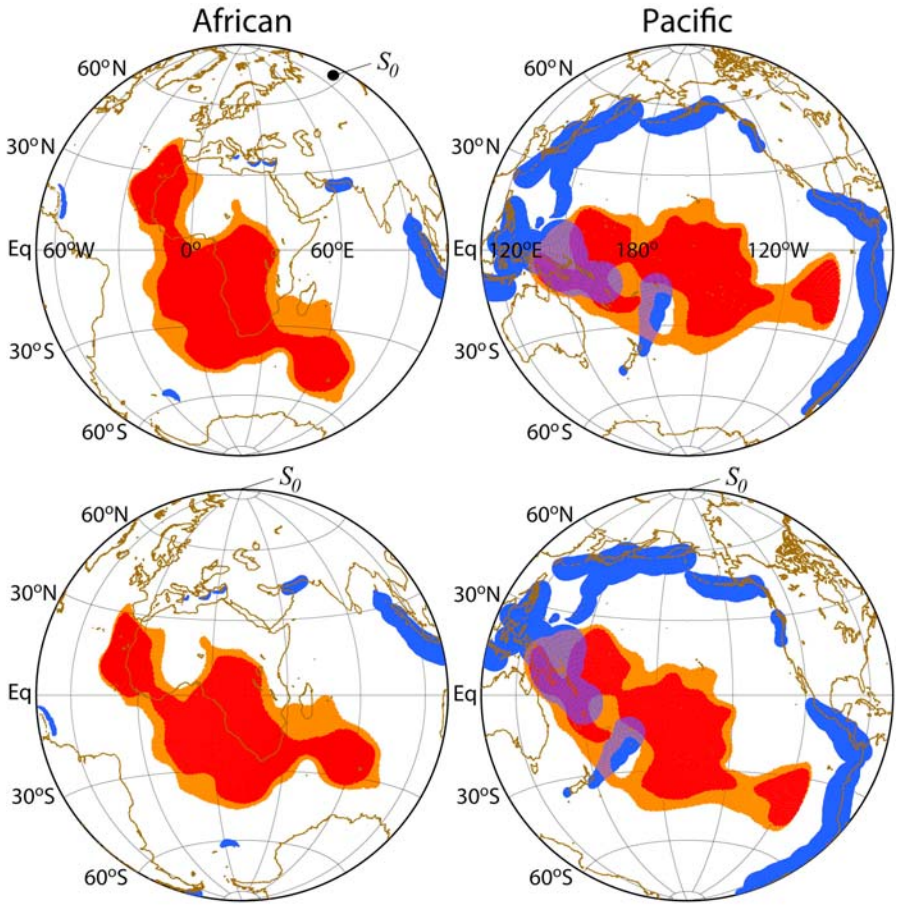

Figure 1. African and Pacific LLSVPs and present-day subduction zones. LLSVPs are indicated as the regions with seismic velocity anomaly less than −1% in the lowermost two layers of the smean [*Becker and Boschi*, 2002] model. Lowermost layer is shown in orange, and second layer from the bottom is shown in red. Locations of subduction are indicated with blue circles, with size corresponding to convergence rate and centers at the plate boundary (trench). (top) Plotted in their present position. (bottom) With projection centers at 11.9°E, 2.7°S, and 168.1°W, 2.7°S, and rotated such that the axis S_0 (96.1°E, 65.6°N) is on top. Continental outlines (also rotated in Figure 1 (bottom)) are shown for orientation.

horizontal gradients in the smean model tend to fall along this contour.

2. Conceptual Model for the Pole Location

[6] Before presenting the full numerical model, we explain the basic concept explored in this paper with a simple geometrical argument. This argument by itself provides no insights beyond the findings of *Hager and Richards* [1989]: They were already able to explain almost 90% of the observed geoid by density anomalies inferred from tomography and a model of subducted slabs. Nevertheless, we find the argument illustrative, as it helps to understand, in a qualitative way, the following results on true polar wander (TPW): In Figure 1 (top), the locations of LLSVPs as well as present-day subduction zones are shown. Because the chemically distinct LLSVPs with long-term stability appear to be mainly in the lowermost ~300 km [*Ishii and Tromp*, 1999; *Burke et al.*, 2008], we approximate them here as consisting of those parts of the bottom two layers of the smean model, with negative s wave speed anomaly in excess of −1% (Figure 1). The bottom mantle layer is below depth 2727 km, the second layer between 2727 km and 2584 km depth. Because the argument given here is merely geometrical, with no dynamics and therefore no topography at the CMB or Earth surface considered yet, it does not matter which densities we assume. For the sake of getting some numbers, we use absolute densities from PREM [*Dziewonski and Anderson*, 1981] at depths 2799 km

and 2655 km, and evaluate the smean model in the bottom two layers on a grid. Corresponding to density, depth range and area assigned to the grid point, we compute a mass for each grid point with s wave anomaly less than −1%. From masses and locations of grid points, we compute the inertia tensor relative to the center of the Earth and obtain LLSVP principal moments 0.77×10^{36} kg m^2 for an axis 11.9°E, 2.7°S, 2.08×10^{36} kg m^2 for an axis 103.1°E, 24.4°S, 2.22×10^{36} kg m^2 for an axis 96.1°E, 65.6°N. Only a fraction of these moments of inertia (which is determined by the density anomaly in and above the LLSVPs, and to what extent this density anomaly is compensated through deflection of the CMB and Earth's surface) contributes to the Earth's nonhydrostatic inertia tensor. However, the relative magnitude of the principal moments and orientation of the axes should not so much depend on these uncertainties. We refer to the last axis as S_0.

[7] In the absence of other contributions, the axis S_0 should be the spin axis. Figure 1 (bottom) shows that if the north pole was at S_0, the major axes of the (very approximately elliptical) African and Pacific LLSVPs have both a very similar orientation relative to the equator, whereas, with the present spin axis, the major axis of the African LLSVP has a much larger angle relative to the equator.

[8] What, then, causes the departure of the spin axis from S_0, in other words, why is the North Pole not in Siberia? We explore here the concept that the pole is shifted to its present location mainly due to the effect of subduction. The two larger principal moments of inertia related to LLSVPs are rather similar: the difference between the largest and intermediate moment of inertia is only about 10% of the difference between the largest and smallest. Hence, in the presence of smaller contributions due to subduction, the spin axis should be able to move rather freely approximately between those two axes, along a great circle that passes close to the present spin axis, and largely avoid the third axis. This third axis at 11.9°E, 2.7°S, as determined here, is virtually identical with a previously found geotectonic bipolarity axis [*Pavoni*, 1985] at 10°E, 0°N. A more natural choice for defining the zero meridian would hence be Trondheim at 10.4°E in the presently adopted coordinate system.

[9] Subducted slabs are, as long as they are in the upper mantle, also associated with geoid highs at spherical harmonic degree 2. Figure 1 shows that areas with the largest amounts of recent subduction (beneath East Asia and South America) and the associated excess masses and geoid highs are, on average, closer to the equator with the actual spin axis than they would be if the spin axis was at S_0. More specifically, the axis of the degree 2 geoid high computed from subduction rates and locations only is at 121.1°E, 12.8°N, but with a spin axis at S_0 it would be at 34.5°N.

[10] Hence the actual spin axis orientation in relation to S_0 can be qualitatively explained due to the Earth orienting itself relative to the spin axis such that excess masses are close to the equator, aligning the spin axis with the axis of maximum nonhydrostatic moment of inertia from all contributions, including LLSVPs and subducted slabs.

[11] By the same token, changes of the spin axis over geologic time relative to the mean mantle, so-called true polar wander (TPW), inferred from paleomagnetic data should be explicable due to changes in the subduction distribution, while LLSVPs and corresponding geoid contributions would have remained more or less constant. No consensus has been reached, though, about occurrence and magnitude of TPW, even for the past 130 Myr. While some groups find TPW, based on models of fixed hot spots [*Besse and Courtillot*, 2002] or slowly moving hot spots [*Steinberger and Torsvik*, 2008], in particular before about 100 Ma, others interpret observations in terms of episodes of faster hot spot motion at several cm/yr [*Tarduno and Gee*, 1995; *Tarduno and Smirnov*, 2001; *Tarduno*, 2007].

[12] Our simple consideration illustrates the basic concept, but reality is more complex in that inferring the geoid, even for the present day requires knowledge of the history of subduction, and the effect of slabs on the geoid at spherical harmonic degree 2 probably reverses from positive in the upper mantle to negative in the lower mantle [*Hager*, 1984; *Ricard et al.*, 1984; *Richards and Hager*, 1984]. Also, lateral viscosity variations, especially due to the slabs with high viscosity, may affect the geoid. While *Richards and Hager* [1989] found that if viscosity variations are less than an order of magnitude globally, the $l = 2$, 3 geoid anomalies are not "seriously contaminated" by lateral viscosity variations, and *Zhang and Christensen* [1993] also found that the $l = 2$ part of the geoid, which is the part relevant for TPW, is not much affected by them, *Zhong and Davies* [1999] found that the high-viscosity slabs have significant effects on the degree 2 geoid. They find that with high-viscosity slabs the degree 2 correlation between predicted and observed geoid is substantially reduced, and hence suggest that slabs in the lower mantle may be no stronger than ambient mantle. On the other hand, *Moucha et al.* [2007] argued that lateral viscosity

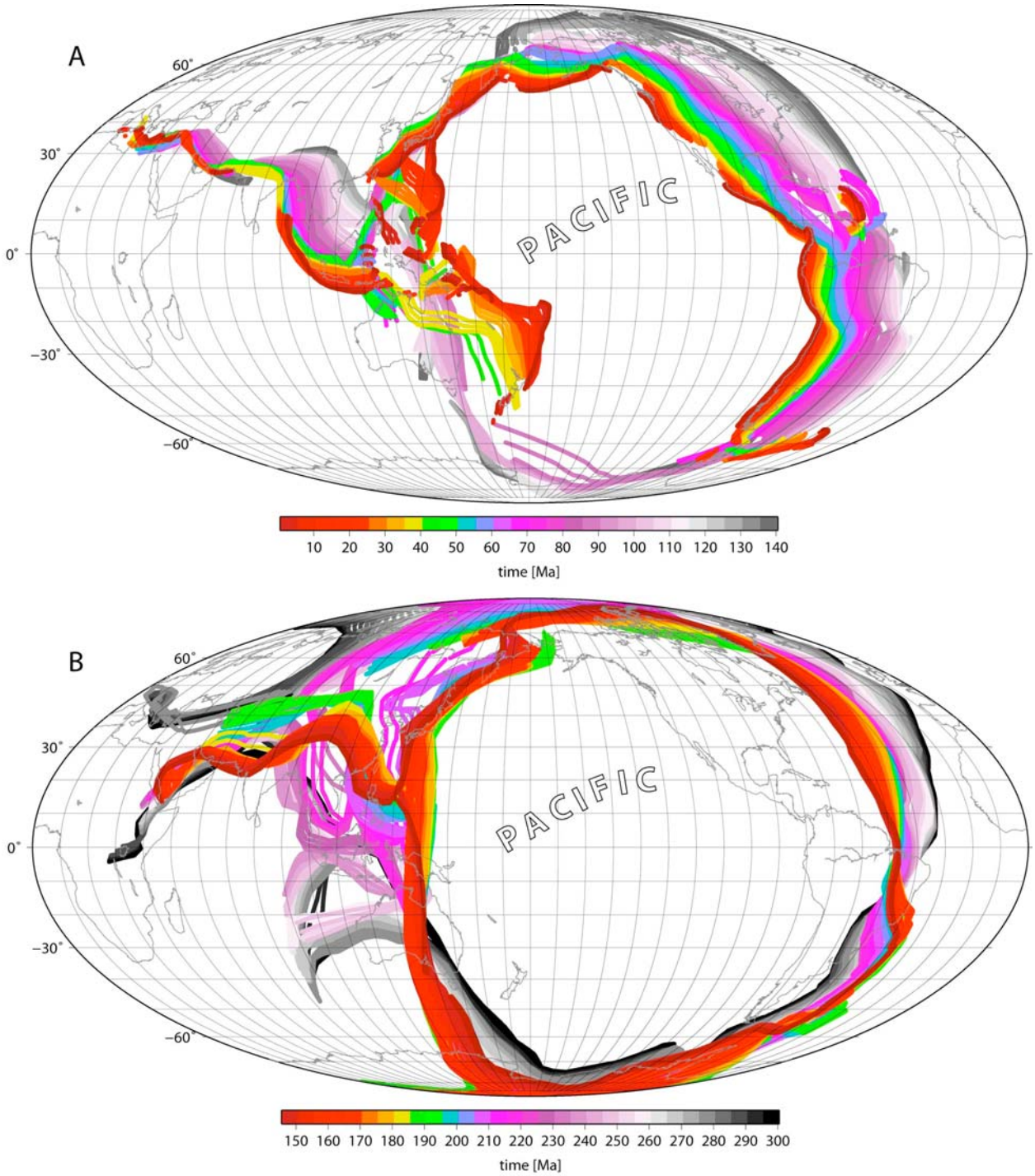

Figure 2. Subduction through time: (a) 0–140 Ma and (b) 142–300 Ma. Subduction zone locations were digitized at 10 Myr intervals based on our global plate reconstructions [*Torsvik et al.*, 2008] in an absolute reference frame corrected for observed TPW [*Steinberger and Torsvik*, 2008] and subsequently interpolated at 2 Myr intervals.

variations inferred from seismic tomography have a minor effect on the geoid. *Ghosh et al.* [2010] further explored this issue.

[13] Furthermore, amplitudes of polar motion are limited by the speed, probably not much more than about 1°/Myr [*Steinberger and O'Connell*, 1997, 2002; *Tsai and Stevenson*, 2007], at which the spin axis can follow changes in the maximum moment of inertia axis imposed by mantle dynamics (henceforth referred to as MMI axis). Hence a misalign-

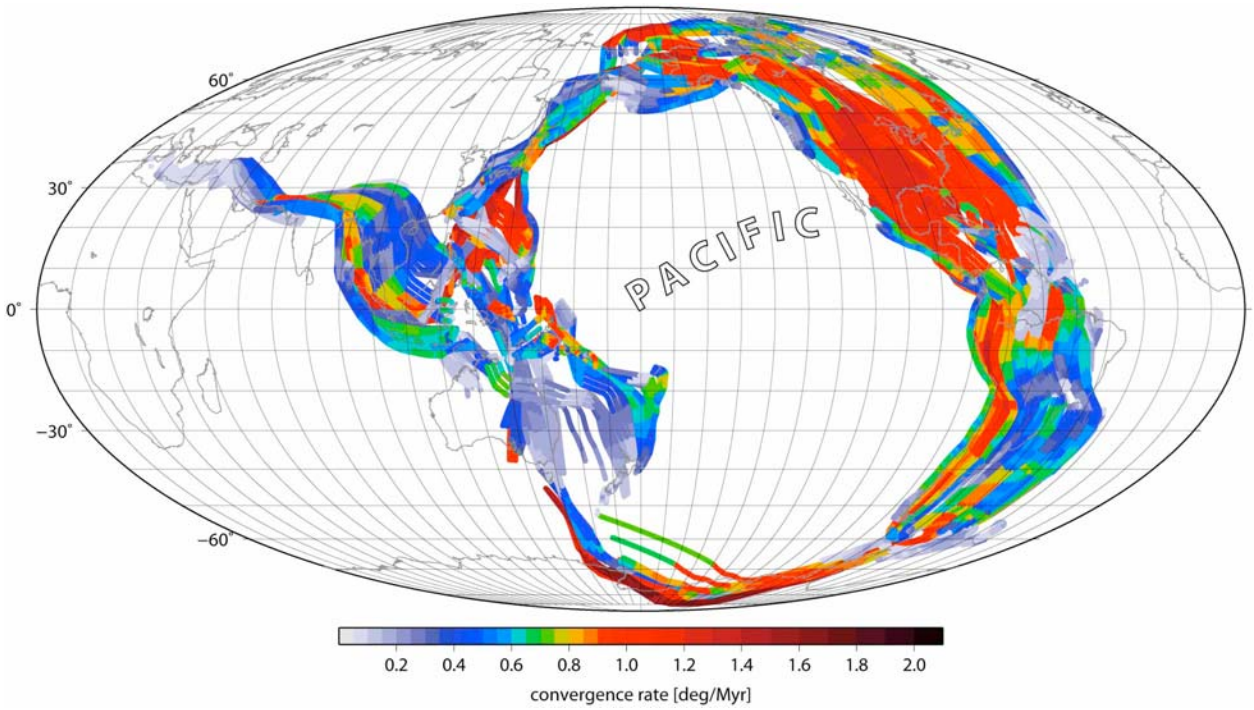

Figure 3. Convergence rates at subduction zones 0–140 Ma. Plates were assigned on either side of the subduction zones, based in part on published paleoage grids [*Müller et al.*, 2008]. Absolute plate motions in the African hemisphere were computed in a moving hot spot reference frame [*Torsvik et al.*, 2008; *Steinberger et al.*, 2004] after 83.5 Ma and a fixed hot spot reference frame [*Torsvik et al.*, 2008; *Müller et al.*, 1993] between 100 and 83.5 Ma. Before 100 Ma we use a paleomagnetic reference frame [*Torsvik et al.*, 2008] corrected for TPW [*Steinberger and Torsvik*, 2008] and with the African plate 9° farther east in order to obtain a fairly smooth transition at 100 Ma. Absolute Pacific plate motions after 83 Ma were independently computed for a model of moving Pacific hot spots [*Steinberger and Gaina*, 2007], whereas a fixed hot spot model [*Duncan and Clague*, 1985] was used before that. Relative plate motions were compiled [*Torsvik et al.*, 2008; *Steinberger and Gaina*, 2007] from a variety of original sources.

ment between the two axes may occur, which causes viscoelastic deformation of the Earth such that the axis of total nonhydrostatic moment of inertia always stays closely aligned with the spin axis.

3. Numerical Model of True Polar Wander

3.1. Subduction History Model

[14] To achieve a more realistic picture than the simple consideration of section 2, we use a subduction history model for the past 300 Myr, derived from a model of plate motions [*Torsvik et al.*, 2008] in an absolute reference frame [*Steinberger and Torsvik*, 2008] (Figure 2) and obtain a model of mantle density, flow, geoid and spin axis location through time. For the past 140 Myr models of Pacific plate motion [*Wessel and Kroenke*, 2008; *Duncan and Clague*, 1985] and paleoage grids [*Müller et al.*, 2008] exist, and we also consider convergence rates (Figure 3) and age (Figure 4) of subducted lithosphere. We assume constant subduction rates either before 140 Ma, or before 175 Ma with smooth transition between 140 and 175 Ma.

[15] Mantle density is computed based on subduction history. Subduction zone locations (Figure 2) were inferred from plate reconstructions [*Torsvik et al.*, 2008; *Steinberger and Torsvik*, 2008; *Torsvik et al.*, 2010]. We use three different models for the amounts of subduction at these subduction zones.

[16] 1. In model 1, plates are assigned on either side of the subduction zones [*Müller et al.*, 2008], and convergence rates (Figure 3) are computed based on models of absolute and relative plate motions [*Torsvik et al.*, 2008; *Steinberger et al.*, 2004; *Müller et al.*, 1993; *Steinberger and Gaina*, 2007; *Duncan and Clague*, 1985] for the past 140 Myr. Also for the past 140 Myr, the age of subducted lithosphere (Figure 4) is inferred from paleoage grids [*Müller et al.*, 2008]. To compute the amount

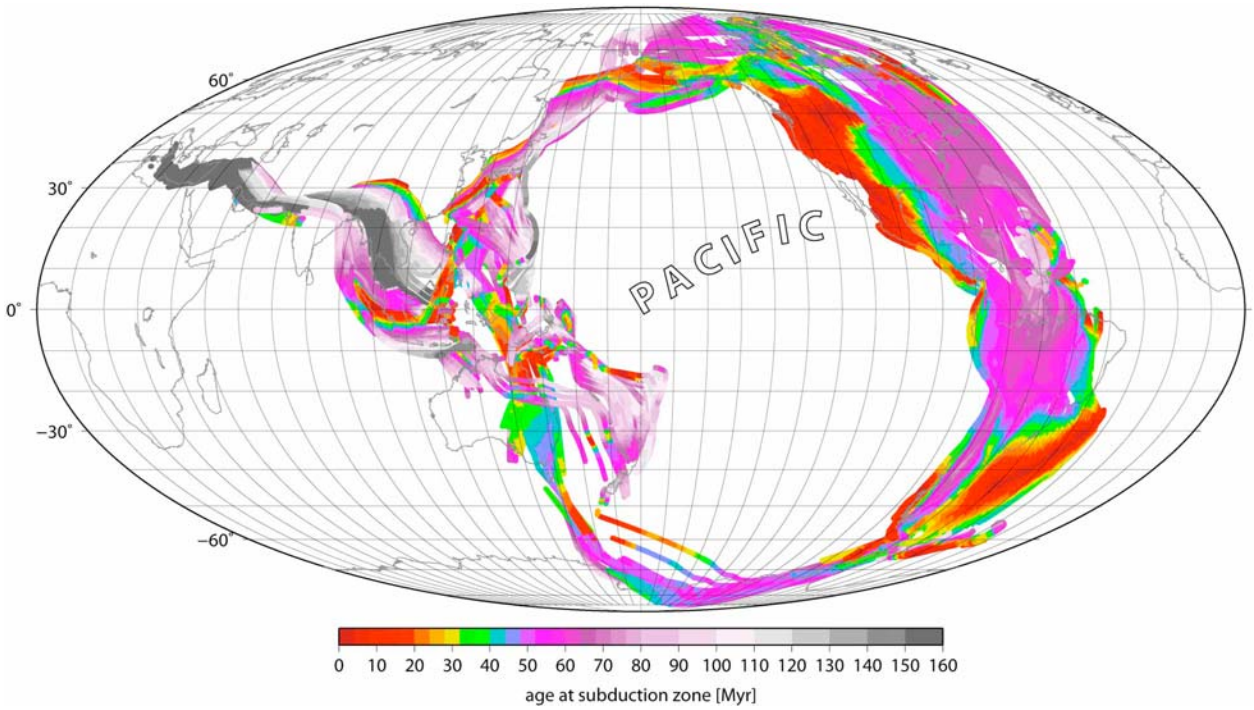

Figure 4. Lithosphere age at subduction zones 0–140 Ma. For each point along a subduction zone, the age of the closest point of the paleoage grid for the corresponding time, on the side of the subducted plate, is used.

of subducted material (in terms of the product of volume and density contrast), the depth-integrated density anomaly of oceanic lithosphere is inferred from the relationship between oceanic age t (Myr) and depth w (km) relative to the mid-ocean ridges $w = 0.35\sqrt{t}$ [*Schubert et al.*, 2001], underlying mantle density 3300 kg/m^3 and seawater density 1020 kg/m^3, assuming isostasy. t is replaced by 80 Myr for $t > 80$ Myr to account for the observed flattening of the age-depth relation. Before 175 Ma, uniform values $t = 80$ Myr and convergence rate 0.4°/Myr are used. Between 140 and 175 Ma, amounts of subduction are linearly interpolated between the variable amounts at 130 Ma and 140 Ma (averaged) and the constant amounts at 175 Ma.

[17] 2. In model 2, a constant $t = 80$ Myr is used for all times. Convergence rates since 140 Ma are computed like in the first model. Before that, a constant convergence rate 0.4°/Myr is used.

[18] 3. In model 3, constant $t = 80$ Myr and convergence rate 0.4°/Myr are used for all times.

[19] Corresponding to the lateral resolution of our flow computation, density anomalies are distributed laterally onto a Gaussian grid, which is suitable for spherical harmonic expansion, with 128 equally spaced longitudes and 64 Gaussian latitudes [*Press et al.*, 1986]. Radially they are distributed onto seven equidistant layers of grid points between 0.92 and 0.98 Earth radii, with relative density anomalies following a Gaussian bell shape (i.e., relative magnitudes $(1 - \sqrt{2}/2)/8$, 1/8, $(1 + \sqrt{2}/2)/8$, 1/4, $(1 + \sqrt{2}/2)/8$, 1/8, $(1 - \sqrt{2}/2)/8$). With this smooth initial density distribution the creation of numerical instabilities is avoided.

[20] Density anomalies corresponding to 2 Myr of subduction are added every 2 Myr in the flow computation. The computation of flow [*Hager and O'Connell*, 1979, 1981] and geoid [*Richards and Hager*, 1984; *Ricard et al.*, 1984] is based on a spherical harmonic expansion, uses free slip upper and lower boundaries and several radial viscosity structures (Figure 5a). Models 1, 2 and 3 (see above) use the same viscosity structure, which is based on mineral physics and optimizing the fit to geoid and other observations [*Steinberger and Calderwood*, 2006]. Viscosities in model 4 are higher than in model 1 by a factor 2 at each depth, yielding identical geoid kernels, and accounting for possibly higher-than-average viscosities beneath regions of long-lasting subduction. Models 5–8 are simplified, with (models 5 and 8) and without (models 6 and 7) a low-viscosity layer in the lowermost mantle, with (models 5,6 and 8) and without (model 7) a low-viscosity asthenosphere. Model 8 also includes a low-viscosity notch between upper and lower

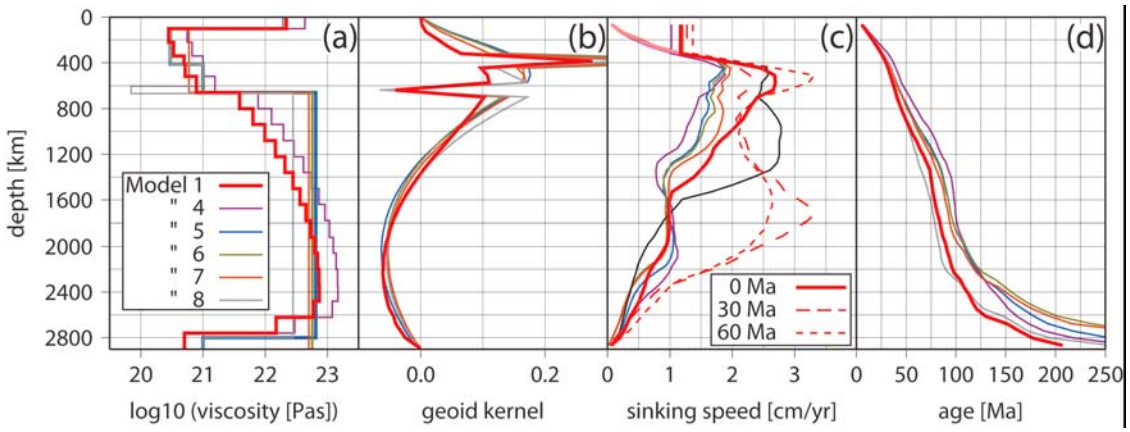

Figure 5. (a) Radial viscosity models used. Model 1 is from *Steinberger and Calderwood* [2006]. (b) Degree 2 geoid kernels. Spikes represent the effect of phase boundaries; their area corresponds to the phase boundary parameters chosen. Kernels for models 1 and 4 are identical. (c) Average sinking speed versus depth for subduction-driven mantle flow with different viscosity models. Sinking speed at a given depth is computed as the average over all points at that depth where the density anomaly is positive and more than 25% of the maximum anomaly at that depth and time. At depth above 300 km, dynamically computed sinking speed (light colored lines, approaching zero toward 0 km depth) is replaced by the value at 319 km (vertical dark colored lines, i.e., constant sinking speed) to account for slabs being primarily kinematically driven in the shallow mantle. Results are for present day, except for model 1, where results for 30 Ma and 60 Ma are additionally shown. (d) Approximate slab age versus depth, computed by integrating the sinking speed versus depth relation (corresponding to dark-colored lines in Figure 5c, but time dependence is considered).

mantle, which enables an improved fit to convection-related observables [*Mitrovica and Forte*, 2004]. All models feature a substantial viscosity increase from the upper to the lower mantle which is generally agreed upon to be required for a good fit to geoid and other convection-related observables. Lateral viscosity variations are not considered. The thermal effect of phase boundaries is also considered [*Steinberger*, 2007], but not the (presumably rather small) latent heat effect resulting from their interaction with the flow. Compressibility is considered [*Panasyuk et al.*, 1996] and a radial gravity and reference density model based on PREM [*Dziewonski and Anderson*, 1981] is used. Figure 5c shows the averaged slab sinking speeds of our models. For model 1, in addition to present day, results for 30 Ma and 60 Ma are shown. The much higher computed sinking speeds at these times in parts of the lower mantle can be attributed to a mid-Cretaceous seafloor spreading pulse [*Seton et al.*, 2009] yielding increased amounts of subduction during that time interval in our model 1. Slabs subducted during the seafloor spreading pulse were in the midmantle at 30 and 60 Ma, but have mostly sunk to the lowermost few 100 km of the mantle at present day according to our model. The time-dependent sinking speed versus depth relation is integrated to obtain an approximate estimate of slab age versus depth. The steep depth versus age model curves in the depth range ~1400–2000 km can again be attributed to the spreading pulse. Based on the geoid kernels (Figure 5b) and the computed density structure, the nonhydrostatic degree 2 geoid and inertia tensor are computed. Advection of absolute density anomalies is done on a grid of 64 × 128 (Gaussian) points laterally and 45 equidistant layers (0.55 to 0.99 Earth radii) radially, using an upwind differencing scheme [*Press et al.*, 1986]. Other effects, such as thermal diffusion (which widens the thermal anomaly but does not affect overall buoyancy), the difference between the adiabatic temperature gradient in the slab and surrounding mantle (which may cause an increase in temperature difference with depth) and a decrease of thermal expansivity with depth are not considered. The latter two effects probably partially compensate each other and, given uncertainties, we regard our approximation as reasonable. In the Appendix, we compare the inferred present-day mantle density structure with seismic tomography along three cross sections (Figure A1).

3.2. Combination of Time-Dependent Density Anomalies Related to Subduction With Constant LLSVPs

[21] Time-dependent density anomalies due to subduction are combined with anomalies related to LLSVPs. As discussed in the introduction, LLSVPs

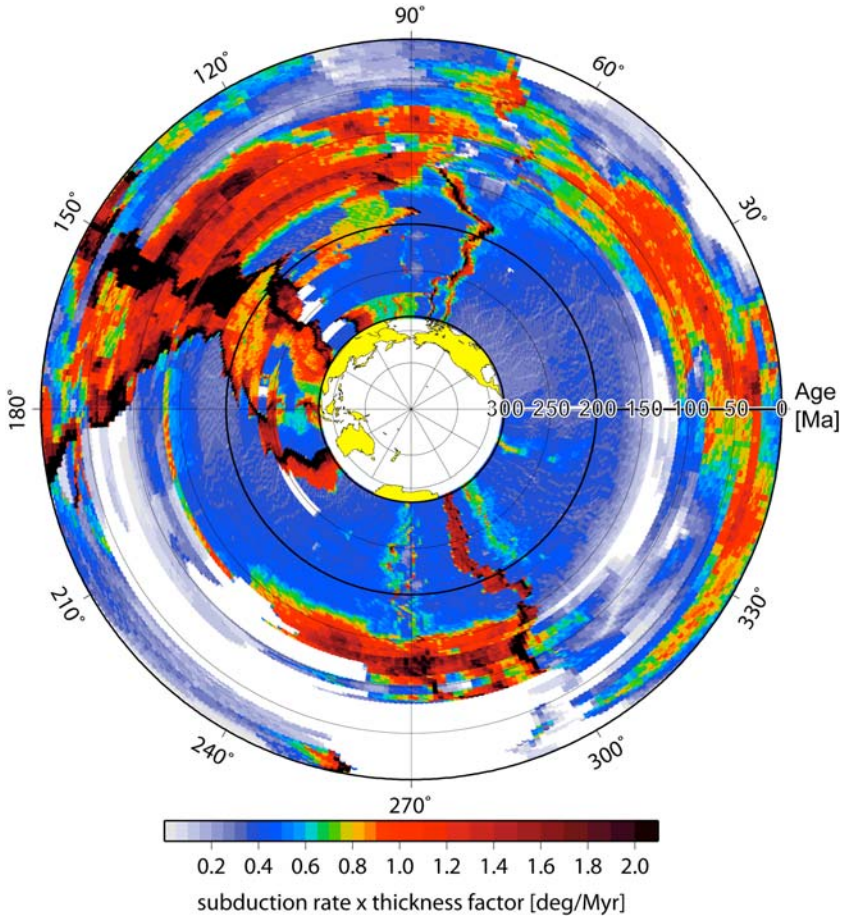

Figure 6. Subduction rate (convergence rate × arc length of subduction zone per degree of azimuth) × lithosphere thickness factor as a function of time (in radial direction outward from 300 to 0 Ma) and azimuth as seen from 0°N, 170°W (center of inset map). From 140 Ma, lithosphere thickness factor is $\sqrt{\text{age of subducted lithosphere}/80\ \text{Myr}}$ for ages ≤80 Myr and 1 otherwise. We use 0.4°/Myr for convergence rate × thickness factor for 176 Ma and earlier, and we interpolate linearly between 140 and 176 Ma. Contributions are added if there are several subduction zones at the same azimuth.

appear to be stable and not buoyantly rising; we hence assume that their geoid contribution does not change with time. The contribution of the LLSVPs, including assumptions on the extent and magnitude of associated density anomalies, is chosen such as to best fit the geoid and thus put the location of the present-day spin axis close to the real poles. Evidently, this ad hoc treatment is unsatisfactory and developing a model that combines mantle flow driven by subducted slabs with stable LLSVPs in a consistent manner remains a challenge.

[22] We assign a relative density anomaly −0.33% (corresponding to a 200–300 K temperature anomaly) to the mantle between ~300 and 1200 km above the CMB above the LLSVPs and obtain a 66% geoid variance reduction for model 1. This is the maximum variance reduction as a function of relative density anomaly, leaving all other model parameters constant. In contrast, zero density anomaly is assumed in the lowermost ~300 km, corresponding to the assumption that the LLSVPs themselves are neutrally buoyant (i.e., chemical and thermal density anomalies compensate each other) but the effect of CMB topography is included. Obviously we could also combine different percentages of density anomalies with different depth ranges, as long as the degree 2 geoid kernel is mainly negative in that range, and maintain a geoid that is identical at degree 2 and very similar overall. We use for all models the same LLSVP geoid contribution (computed for model 1). This simplified approach is justified, because with a relative density anomaly that is only slightly (given the similarity of degree 2 kernels) changed, again a geoid that is identical at degree 2 and very similar

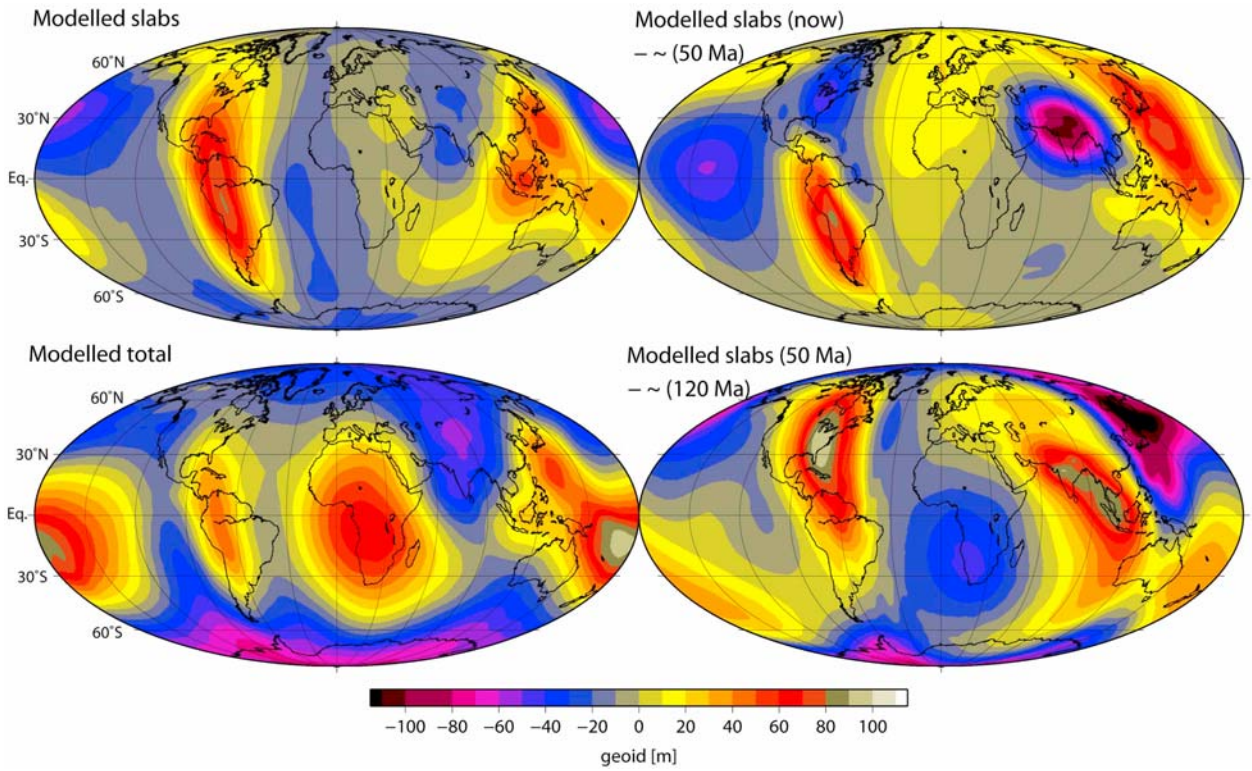

Figure 7. Modeled geoid (viscosity and subduction history model 1), expanded up to degree 31. (top left) Slab contribution only. (bottom left) LLSVP plus slab contributions. (top right) Modeled geoid change over the past 50 Myr. (bottom right) Modeled change from 120 Ma to 50 Ma.

overall (given the degree 2 dominance of the LLSVP geoid contribution) could be achieved.

[23] For our model predictions to be meaningful, the model should also fit the present-day geoid well. However, this can only be assessed after a 300 Myr model run, and the geoid is quite sensitive to viscosity structure. Results for model 1 were achieved without iterations, and for viscosity models 5–8 we choose the lower mantle viscosity value in each case such that in combination with the present-day density structure predicted for model 1, variance reduction is maximized. In this way, we expect a comparatively good fit to the present-day geoid also when flow and density structure is computed with the same viscosity model as the geoid. We obtain variance reduction between 36% for model 5 and 72% for model 8 (but only 24% for model 4).

3.3. Relation of Time-Dependent Density Anomalies and True Polar Wander

[24] To compute the orientation of the spin axis as a function of time, we first compute the axis of maximum moment of inertia as imposed by mantle dynamics (MMI axis) versus time. When the latter axis changes, nondiagonal inertia tensor elements J_{xz} and J_{yz} develop in a coordinate system where the z axis is aligned with the spin axis. The rotation axis then changes its orientation at a rate that is proportional to these [*Steinberger and O'Connell*, 1997]:

$$\frac{d\omega_x}{dt} = c_{tpw}\omega_0 J_{xz} \qquad \frac{d\omega_y}{dt} = c_{tpw}\omega_0 J_{yz}$$

where ω_0 is the diurnal rotation rate and c_{tpw} is a constant that mainly depends on the Earth's viscosity structure. From the results shown by *Steinberger and O'Connell* [1997, Figure 2], we estimate for the viscosity structure used here [*Steinberger and Calderwood*, 2006] a value of approximately 10°/Myr/10^{33} kg m^2, which we will use here. The spin axis remains approximately aligned with the MMI axis, if the latter changes sufficiently slowly.

4. Pole Location From 300 Myr of Subduction

[25] The pole is expected to remain close to a great circle 90° from the geotectonic bipolarity axis marking the presumed two antipodal stable large-scale upwellings [*Evans*, 2003] and this is also

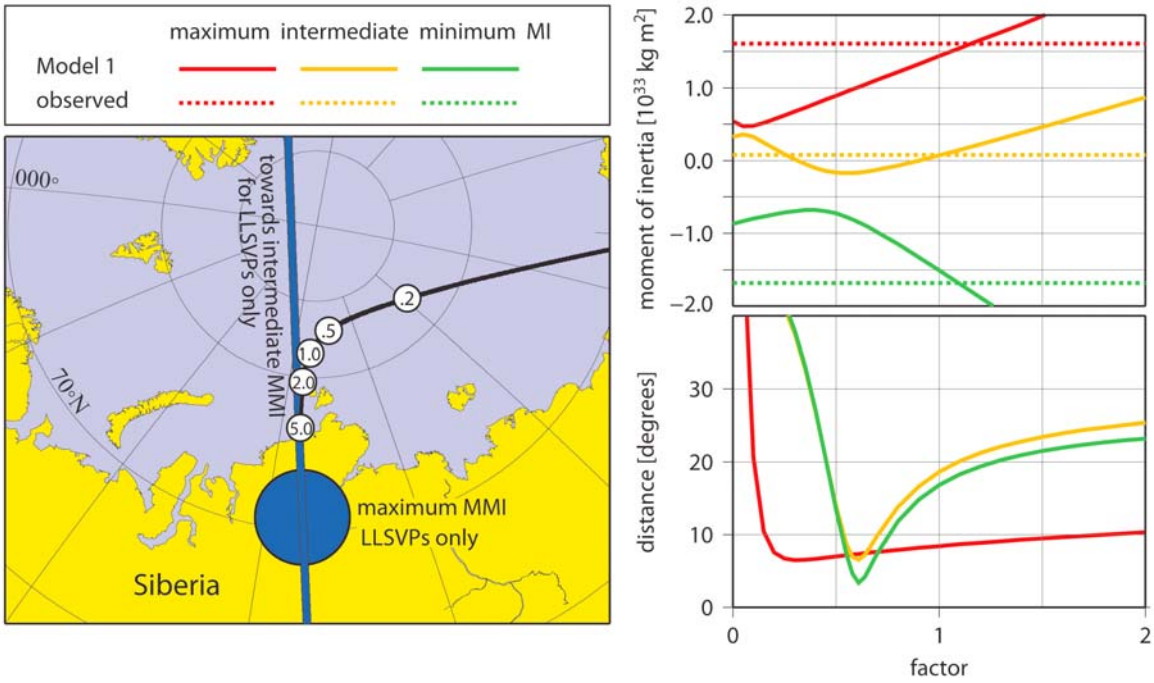

Figure 8. Fit between predicted and observed inertia tensor for different "weight factors" indicating the relative magnitude of the LLSVP geoid contribution. A factor of 1 corresponds to the optimum fit as in Figure 7 (bottom left). Viscosity and subduction history model 1 is used. (left) White circles indicate predicted present pole location for different "weight factors," whereas the large blue circle shows the axis of maximum moment of inertia due to LLSVPs only (computed from only the bottom layer of the smean model, hence in a slightly different location than S_0, indicating uncertainties due to details of modeling assumptions). The blue line runs toward the axis of intermediate moment of inertia due to LLSVPs. (top right) Modeled (continuous lines) and observed (dotted lines) nonhydrostatic moments of inertia. (bottom right) Distance (in degrees) between modeled and observed principal axes of the inertia tensor.

found for TPW derived from paleomagnetism, in combination with models of slowly moving, or fixed hot spots [*Steinberger and Torsvik*, 2008; *Besse and Courtillot*, 2002]. Hence it is instructive to show subduction as a function of time and azimuth, as seen from the geotectonic bipolarity axis (similar to the LLSVP centers) (Figure 6). With average slab sinking speeds inferred from our subduction-driven mantle flow model (Figure 5c) we expect that at spherical harmonic degree 2, slabs should cause a positive geoid for about 75 Myr after subduction, and a negative geoid after that, because the degree 2 geoid kernel changes from positive in the upper part of the mantle to negative in the lower part (Figures 5b and 5d). However, our model indicates large lateral and temporal variations in slab sinking speed, and hence the time after which the effect on the degree 2 geoid reverses sign.

[26] Figure 7 (top left) shows the resulting present-day geoid resulting from subduction over the past 300 Myr for model 1. Although only the degree 2 geoid is relevant for the spin axis, the relation to subduction becomes clearer, if the geoid is shown to a higher degree. Essentially our conceptual model is confirmed in that geoid highs are predicted over the regions with the largest amounts of recent subduction, East Asia (~150° azimuth in Figure 6) and South America (~340° azimuth). These geoid highs are much farther from the actual pole than from S_0, consistent with the consideration that the Earth orients itself relative to the spin axis to move excess masses and corresponding geoid highs as far as possible away from the poles.

[27] The geoid due to subduction is combined with a contribution due to LLSVPs such that an optimum fit to the observed geoid is obtained (Figure 7, bottom left). For the combined geoid, the MMI axis is much closer to the actual pole than S_0 is, at about 82°N and longitude similar to S_0 for model 1, and between 74°N and 88°N, remaining close to the dark green line, for all models. Furthermore, for model 1 the modeled and observed nonhydrostatic inertia tensor also agree well; principal inertia tensor axes

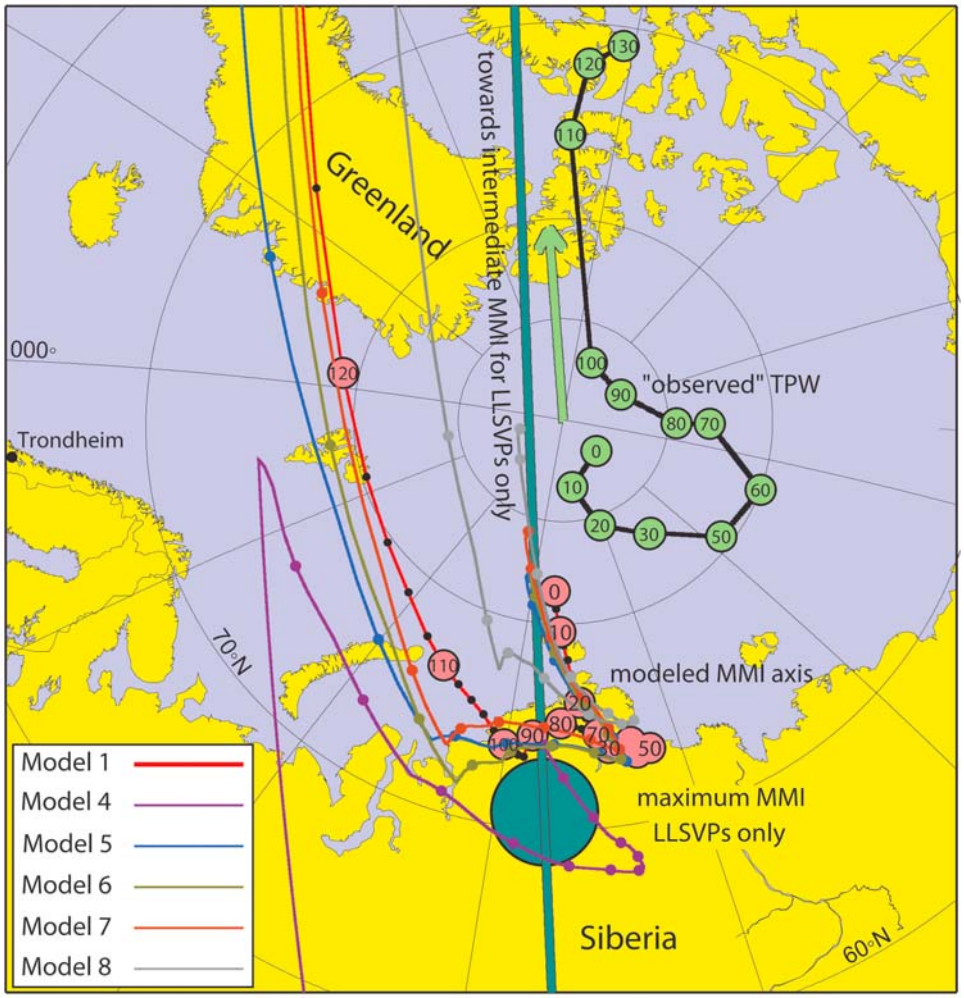

Figure 9. MMI axis predicted from subduction history/viscosity model 1 (red circles) and observed polar wander in the "global mantle" reference frame (green circles) [*Torsvik et al.*, 2008]. Corresponding model results for other viscosity structures are shown as colored lines with dots in 10 Myr intervals. The dark green circle shows the axis of maximum moment of inertia due to LLSVPs only. The dark green line runs toward the axis of intermediate moment of inertia due to LLSVPs. The green arrow indicates the geodetically observed polar motion [*Gross and Vondrák*, 1999].

(including the spin axis) are fit somewhat better when giving a lower weight to the LLSVP contribution (Figures 8 (left) and 8 (top right)), whereas principal moments are fit somewhat better with slightly higher weight (Figure 8, bottom right). Independent of the exact weight, Figure 8 illustrates that both contributions, due to slabs and LLSVPs, are required to obtain a good fit to inertia tensor and rotation axis.

5. Subduction Changes and True Polar Wander

[28] With the same subduction history model we can infer a model of the spin axis as a function of time. Again, the azimuthal diagram in Figure 6 in combination with the approximate rules that (1) subduction should lead to a positive geoid for 50 Myr, followed by a negative geoid afterward, and (2) polar wander tends to move geoid highs to the equator and lows to the pole, should give us a qualitative understanding of geoid changes and TPW, which is then refined by the full numerical computations of the MMI axis and the spin axis considering rotational dynamics.

[29] Figure 6 shows for the most recent past (50 Myr or less) an increase in subduction around 150° azimuth (corresponding to East Asia) and 340° azimuth (South America), and a decrease around 30° azimuth (North America). Hence we expect a geoid increase in East Asia and South America and a decrease in North America. The

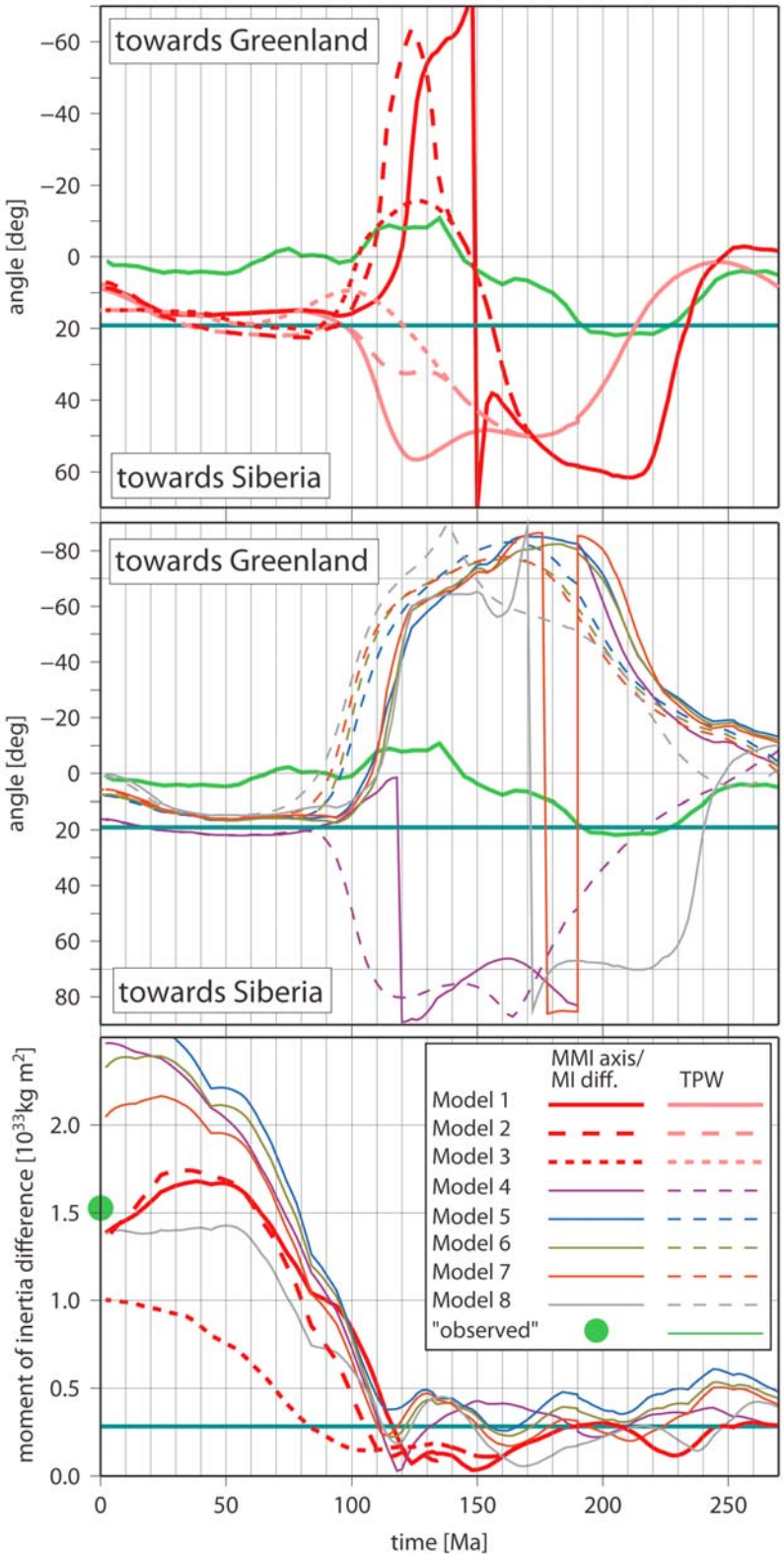
towards Greenland
towards Siberia
angle [deg]
towards Greenland
towards Siberia
angle [deg]
MMI axis/
MI diff.
TPW
Model 1
Model 2
Model 3
Model 4
Model 5
Model 6
Model 7
Model 8
"observed"
moment of inertia difference [10^33 kg m^2]
time [Ma]

Figure 10

numerical model confirms this expectation (Figure 7, top right); a motion of the MMI axis and spin axis toward Greenland is computed for all viscosity models considered, in agreement with observed TPW (Figures 9 and 10).

[30] Between 120 Ma and 50 Ma, amounts of subduction have decreased in polar latitudes (~90° and 270° in Figure 6), hence the geoid is generally predicted to have gone down there. In contrast, amounts have increased in equatorial latitudes, where hence the geoid is generally predicted to have gone up (Figure 7, bottom right). Figure 10 (bottom) shows that this geoid change has caused an increase in the predicted difference between maximum and intermediate moment of inertia after about 120 Ma, reaching values close to the observed present-day difference after about 70 Ma for model 1, and 60–80 Ma for all viscosity models. This much larger difference can explain that after about 100 Ma the spin axis appears to have remained more stable than before, and is expected to have closely followed the maximum moment of inertia axis imposed by mantle dynamics. With a smaller difference between maximum and intermediate moment of inertia, small changes in mantle density distribution can cause much larger changes of the MMI axis in the plane of the maximum and intermediate moment of inertia, and a substantial misalignment between spin axis and MMI axis.

[31] When varying the amount of LLSVP contribution for model 1, as illustrated in Figure 8, predicted TPW curves stay similar; somewhat less motion is predicted for a larger LLSVP contribution, and vice versa.

[32] As an aside, we note that for the model corresponding to the continuous red line in Figure 10 (bottom), the maximum nonhydrostatic moment of inertia has increased from 1.10×10^{33} kg m^2 at 124 Ma to a maximum value 1.65×10^{33} kg m^2 at 56 Ma, and decreased again to 1.38×10^{33} kg m^2 at present. Compared to the Earth's total moment of inertia, this corresponds to an increase by a fraction 0.68×10^{-5} followed by a decrease by 0.33×10^{-5}. With constant present-day angular momentum, this would correspond to an increase in the length of day by 0.6 s followed by a decrease by 0.3 s. Hence the implied length of day variations are quite negligible compared to the secular slowdown due to tidal friction.

[33] Also from 120 to 50 Ma, in contrast to the most recent past, we expect the geoid to have risen in North America, where large amounts of slabs have been subducted in that time interval, and gone down in Asia (90–150° in Figure 6) where subduction rates after 60–70 Ma became less than before. Again, our numerical model confirms this expectation (Figure 7, bottom right), hence a motion of the MMI axis toward Siberia is computed for all viscosity models considered, again in agreement with observed TPW (Figures 9 and 10). The predicted motion of the spin axis (Figure 10), though, does not follow this direction in several of the cases considered. This discrepancy may indicate that the difference between maximum and intermediate moment of inertia before ~120 Ma was larger than in our model (although probably smaller than at present), leading to slower motion of the MMI axis and closer alignment with the spin axis.

6. Discussion

[34] Both paleomagnetically derived TPW and predicted movement of the MMI axis and spin axis tend to follow the line connecting maximum and intermediate moment of inertia due to LLSVPs (Figure 9). This has also been noted by *Pavoni* [2008] for the geodetically observed polar motion [*Gross and Vondrák*, 1999]. Hence even the geodetical polar motion, which is probably caused by postglacial rebound during the last 10,000 years and faster than longer-term polar wander, appears to be restricted to closely follow this great circle [*Pavoni*, 2008]. For our preferred viscosity model, the computed MMI axis agrees with "observed"

Figure 10. (top) TPW inferred from paleomagnetic reference frame (light green) [*Steinberger and Torsvik*, 2008] and modeled motion of the MMI axis (red) and spin axis (pink) along the dark green line. Continuous lines consider variations in ocean floor ages and subduction rates since 140 Ma (model 1), long-dashed lines are for constant ages but variable subduction rates after 140 Ma (model 2), and short-dashed lines are for constant ages and constant subduction rates for all times (model 3). Viscosity structure is the same as in model 1 for all three cases. Horizontal dark green line corresponds to predicted spin axis location from LLSVPs only. The abrupt shift in the continuous red line at 150 Ma represents an "inertial interchange" event when the two larger principal moments of inertia become nearly equal. (middle) As in Figure 10 (top) but for different viscosity models 4–8. (bottom) Modeled difference between maximum and intermediate moment of inertia. Long-dashed and short-dashed lines are for the same cases as in Figure 10 (top). Green dot represents observed present-day difference. Horizontal dark green line corresponds to contribution related to LLSVPs only.

TPW regarding the time periods when the axis is displaced toward Greenland or toward Siberia relative to its present location (Figure 10, top). This result is independent of whether or not the seafloor ages of subducted lithosphere are considered (continuous versus dashed lines). Qualitatively the same result is obtained even if convergence rates are not considered, based only on subduction zone locations (dotted lines). Our results can also explain the smaller amounts of true polar wander during the past ~100 Myr due to a larger difference between maximum and intermediate moments of inertia. However, before ~120 Ma amounts of motion and displacement computed for the MMI axis are substantially larger than observed rates and amounts of true polar wander, and the predicted difference between MMI axis and spin axis (pink lines in Figure 10, top) can be quite large. Again, if the difference between maximum and intermediate moment of inertia before ~120 Ma was larger than in our model, slower motion of the MMI axis and closer alignment with the spin axis would result, possibly leading to better agreement between paleomagnetically derived TPW and predicted motion of the MMI axis and spin axis. The discrepancies for these earlier times are at least partly due to large uncertainties in the amounts of subduction before ~130 Ma.

[35] Figure 10 (top) shows that following very fast changes of the MMI axis (several tens of degrees/Myr), the predicted changes of the spin axis reach up to about 2°/Myr, about twice as much as previous theoretical estimates [*Steinberger and O'Connell*, 1997, 2002; *Tsai and Stevenson*, 2007]. Interpretation of paleomagnetic results in terms of TPW speed leads to widely discrepant results. Based on paleomagnetic results from the Indo-Atlantic, the TPW models of *Besse and Courtillot* [2002], *Torsvik et al.* [2008], and *Steinberger and Torsvik* [2008] do not exceed about 1°/Myr. However, *Prévot et al.* [2000] conclude from Indo-Atlantic data that around 110 Ma, during a 20° abrupt tilting speeds exceeding 5°/Myr may have been reached, and *Sager and Koppers* [2000] infer from the magnetic field above Pacific seamounts that a rapid polar wander episode with 3 to 10°/Myr may have occurred around 84 Ma. In contrast, *Tarduno and Gee* [1995], *Cottrell and Tarduno* [2000], *Tarduno and Smirnov* [2001], and *Tarduno* [2007] do not see evidence for TPW at all, and rather interpret observations in terms of episodes of faster hot spot motion at several cm/yr. Large and fast TPW events may have occurred in the more distant geological past: *Kirschvink et al.* [1997] find evidence for inertial interchange TPW (90° in about 10 Myr) in the early Cambrian, and *Maloof et al.* [2006] conclude that their observations are best explained by rapid TPW events (with apparent plate motions of 54–270 cm/yr) around 800 Ma. Such fast TPW events would require faster changes of the MMI tensor and/or faster viscoelastic adjustment of the equatorial bulge than in our model, and would presumably require lower viscosities in the mantle.

[36] Qualitatively, we can explain polar motion as caused by changes in subduction around the Pacific. A possibly important aspect is that there used to exist a plate ("Izanagi") in the northwest Pacific basin that has now been completely subducted. Paleoage grids [*Müller et al.*, 2008] indicate that the Pacific-Izanagi ridge gradually approached the northwest Pacific subduction zone until the ridge itself was subducted at around 60 Ma, then the Izanagi plate disappeared and the Pacific plate itself was subsequently subducted. Thus overall motion of the pole toward Asia between 130 and 50 Ma may be due to a reduction of subduction beneath East Asia during that time period, hence the geoid going down, as the age of the Izanagi plate at the subduction zone gradually became younger, and the convergence rate became smaller when the Pacific plate was subducted instead of the Izanagi plate. Conversely, an overall motion away from Asia between 200 and 130 Ma could be due to increasing amount of subduction beneath East Asia. We hypothesize that before ~200 Ma, subduction was approximately equal all around the Panthalassa Ocean basin which surrounded Pangea and which developed into the Pacific, but through time an asymmetry developed whereby the Izanagi plate, in the northwestern Pacific basin, moved and was subducted at increasingly faster rates. Such qualitative explanations should, however, be regarded as tentative, because, for example, for our preferred viscosity model the same episodes of MMI axis displacement are predicted even if changes in subduction rate and plate age at subduction zones are completely disregarded, based only on changes in subduction zone geometry.

[37] Polar motions over geologic time are likely caused by changes in mantle density. These polar motions have caused large changes in latitude, for example, up to 28° between 195 and 135 Ma, also affecting regional sea level [*Mound and Mitrovica*, 1998] and climate. For the more recent geologic past, such changes can be computed based on a backward advection of present-day mantle density anomalies [*Steinberger and O'Connell*, 1997, 2002]. This approach probably cannot be used for more than 70 Myr, however, recently developed inverse

approaches [*Bunge et al.*, 2003; *Liu et al.*, 2008] promise to push this limit farther back in time. Here we have developed an alternative approach: modeling changes in the inertia tensor and polar motion due to contributions from LLSVP with long-term stability and contributions from subduction that change over time. The resulting density and flow model gives a reasonable fit to the geoid (66.5% variance reduction for degrees 1–31) and, when combined with a more realistic model of the lithosphere, plate motions can be predicted quite well (S. V. Sobolev et al., manuscript in preparation, 2010). A previous geodynamic model of changes of the Earth's spin axis due to subduction history [*Richards et al.*, 1997] did not consider the effect of LLSVPs with long-term stability, which has been considered only more recently [*Zhong et al.*, 2007; *Rouby et al.*, 2010]. The approach of *Rouby et al.* [2010] is similar to ours in that they also compute TPW from geoid changes due to a combination of time-variant subduction and time-invariant upwellings. But their model of upwellings is different, yielding an MMI axis that is already close to the north pole. When adding the subduction contribution, their total present-day MMI axis shifts in the same direction as for us and is on the Canadian side of the North Pole. In our model, it is still on the Siberian side, which suggest that the most realistic case maybe somewhere between the two models. Without modifying the subducted slab model, the two approaches qualitatively agree on the predicted direction of polar motion since 50 Ma and on how the difference between maximum and intermediate moment of inertia evolves since 50 Ma. More generally, in both models the MMI axis tends to follow the line at 90° from the minimum moment of inertia axis due to upwellings or LLSVPs only (dark green line in Figure 10). However, before 50 Ma, predicted changes of the MMI axis disagree, presumably due to larger differences in the respective subduction history models used before 120 Ma. Results on which both models agree can be regarded as the most robust.

[38] Whereas subduction of lithospheric plates has long been recognized as an important and time-dependent contribution to mantle convection, and hence an important cause of TPW, it has recently become more evident that the LLSVPs of the Earth's lowermost mantle add long-term stability to the mantle system. We have shown here that the combination of mantle density anomalies due to subduction and LLSVPs is suitable to model large-scale features of the geoid, and hence the Earth's present-day inertia tensor and spin axis orientation. Extending our approach to the past, we are able to explain essential features of TPW as caused by changes in mantle density anomalies due to subduction, while density anomalies related to LLSVPs remained largely unchanged. Adding other time-dependent features such as mantle plumes, and improving models of subduction will change predicted TPW. At the same time, the models should be consistent with independent evidence of slab sinking speed versus depth [*van der Meer et al.*, 2010]. Our models predict somewhat larger sinking speeds than found by *van der Meer et al.* [2010]. Our results also indicate that this discrepancy can probably be reduced if lateral viscosity variations, with higher viscosities in regions of abundant subduction over the past few hundred Myr, are considered. Models should also maintain a good fit for the present-day long-wavelength geoid, with the predicted MMI axis close to the poles. These requirements make the modeling quite challenging, as the fit can be only evaluated after the 300 Myr model run, and the predicted geoid and MMI axis are quite sensitive to details of the viscosity and density structure. A systematical study of which kinds of viscosity structures satisfy these requirements, and an evaluation of what are the robust features of predicted TPW, and what are the variations, among "acceptable" viscosity models is hence not attempted here. However, for different viscosity models shown, the predicted MMI axis always moves faster before ~100 Ma, it moves toward Siberia until about 50–80 Ma, and then reverses direction toward Greenland. These features also agree with observed TPW and together with the fact that independent of details of the numerical model, they can already be qualitatively understood based on the "azimuthal diagram" in Figure 6, there is a strong indication that they are real. Another challenge for future models is to self-consistently explain the long-term stability of LLSVPs.

7. Conclusions

[39] Uncertainties in model assumptions and subduction history make it still challenging to compute true polar wander through geologic history. Nevertheless, our novel model captures and explains, for the first time, some essential features of the Earth's rotational dynamics over the past 300 Myr. Our results indicate the following: (1) Motion of the pole toward Greenland over the past 50 Myr is caused by increased amounts of subduction beneath

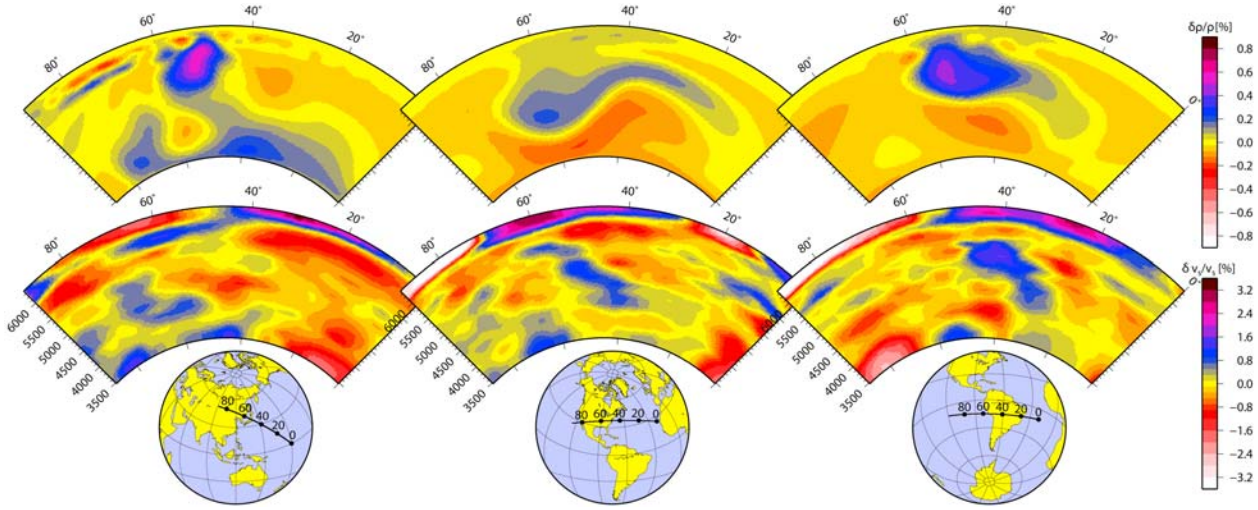

Figure A1. Comparison of (top) modeled present-day mantle density structure based on 300 Myr of subduction (model 1) with (bottom) a recent tomography model [*Simmons et al.*, 2006] along three cross sections.

East Asia and South America, and decreased amounts beneath North America since then. (2) Motion of the pole toward Siberia before that is caused by large amounts of subduction beneath North America between ~120 and 50 Ma and decreasing amounts of subduction in East Asia after 60–70 Ma. (3) Greater stability of the spin axis during the past ~100 Myr is caused by a decrease in the amount of subduction in polar latitudes, and an increase in equatorial latitudes.

Appendix A: Comparison of Predicted Density Anomalies With Tomography

[40] Figure A1 illustrates the inferred present-day density structure along three cross sections and compares it with a tomography model. Differences are substantial, in particular, although both the tomography model and our density model are expanded up to spherical harmonic degree 63, the tomography model shows more higher-resolution features. Obtaining a better agreement between density models inferred from subduction history and from tomography will be a major challenge for future research. Discrepancies may be partly due to inaccuracies of the subduction history model, partly due to modeling simplifications (e.g., slabs are more viscous than surrounding mantle, and may therefore remain more narrow and slab-like than in the model) and partly due to uncertainties in the tomography model and the fact that seismic velocity heterogeneities do not always correspond to density heterogeneities. Nevertheless, we maintain for the purpose of this paper, where only the largest-scale (degree 2) density structure is relevant, that our density model is appropriate.

Acknowledgments

[41] Funding was provided by NFR and StatoilHydro. We thank Susanne Buiter and Carmen Gaina; the Editor, John Tarduno; reviewers Shijie Zhong and Jon Mound; and an anonymous reviewer for comments. Figures 1–10 and A1 were prepared using the GMT [*Wessel and Smith*, 1998] software.

References

Becker, T., and L. Boschi (2002), A comparison of tomographic and geodynamic mantle models, *Geochem. Geophys. Geosyst.*, *3*(1), 1003, doi:10.1029/2001GC000168.

Besse, J., and V. Courtillot (2002), Apparent and true polar wander and the geometry of the geomagnetic field over the last 200 Myr, *J. Geophys. Res.*, *107*(B11), 2300, doi:10.1029/2000JB000050.

Bunge, H.-P., C. R. Hagelberg, and B. J. Travis (2003), Mantle circulation models with variational data assimilation: Inferring past mantle flow and structure from plate motion histories and seismic tomography, *Geophys. J. Int.*, *152*, 280–301.

Burke, K., B. Steinberger, T. H. Torsvik, and M. A. Smethurst (2008), Plume generation zones at the margins of large low shear velocity provinces on the core-mantle boundary, *Earth Planet. Sci. Lett.*, *265*, 49–60.

Cottrell, R. D., and J. A. Tarduno (2000), Late Cretaceous true polar wander: Not so fast, *Science*, *288*, 2283.

Crough, S. T., and D. M. Jurdy (1980), Subducted lithosphere, hotspots, and the geoid, *Earth Planet. Sci. Lett.*, *48*, 15–22.

Duncan, R. A., and D. A. Clague (1985), Pacific plate motion recorded by linear volcanic chains, in *The Pacific Ocean, The Ocean Basins and Margins*, vol. 7A, edited by A. E. A. Nairn, F. L. Stehli, and S. Uyeda, pp. 89–121, Plenum, New York.

Dziewonski, A. M., and D. L. Anderson (1981), Preliminary reference Earth model, *Phys. Earth Planet. Inter.*, *25*, 297–356.

Evans, D. A. D. (2003), True polar wander and supercontinents, *Tectonophysics*, *362*, 303–320.

Fukao, Y., S. Widiyantoro, and M. Obayashi (2001), Stagnant slabs in the upper and lower mantle transition region, *Rev. Geophys.*, *39*, 291–323.

Garnero, E. J., T. Lay, and A. K. McNamara (2007), Implications of lower mantle structural heterogeneity for existence and nature of whole mantle plumes, *Spec. Pap. Geol. Soc. Am.*, *430*, 79–102.

Ghosh, A., T. W. Becker, and S. J. Zhong (2010), Effects of lateral viscosity variations on the geoid, *Geophys. Res. Lett.*, *37*, L01301, doi:10.1029/2009GL040426.

Gold, T. (1955), Instability of the Earth's axis of rotation, *Nature*, *175*, 526–529.

Goldreich, P., and A. Toomre (1969), Some remarks on polar wandering, *J. Geophys. Res.*, *74*, 2555–2569.

Grand, S. P. (2002), Mantle shear-wave tomography and the fate of subducted slabs, *Philos. Trans. R. Soc. London, Ser. A*, *360*, 2475–2491.

Grand, S. P., R. D. van der Hilst, and S. Widiyantoro (1997), Global seismic tomography: A snapshot of convection in the Earth, *GSA Today*, *7*, 1–7.

Gross, R. S., and J. Vondrák (1999), Astrometric and space-geodetic observations of polar wander, *Geophys. Res. Lett.*, *26*, 2085–2088.

Hager, B. H. (1984), Subducted slabs and the geoid: Constraints on mantle rheology and flow, *J. Geophys. Res.*, *89*, 6003–6015.

Hager, B. H., and R. J. O'Connell (1979), Kinematic models of large-scale flow in the Earth's mantle, *J. Geophys. Res.*, *84*, 1031–1048.

Hager, B. H., and R. J. O'Connell (1981), A simple global model of plate dynamics and mantle convection. *J. Geophys. Res.*, *86*, 4843–4867.

Hager, B. H., and M. A. Richards (1989), Long-wavelength variations in Earth's geoid: Physical models and dynamical implications, *Philos. Trans. R. Soc. London, Ser. A*, *328*, 309–327.

Hager, B. H., R. W. Clayton, M. A. Richards, R. P. Comer, and A. M. Dziewonski (1985), Lower mantle heterogeneity, dynamic topography and the geoid, *Nature*, *313*, 541–545.

Ishii, M., and J. Tromp (1999), Normal-mode and free-air gravity constraints on lateral variations in velocity and density of the Earth's mantle, *Science*, *285*, 1231–1236.

Kirschvink, J. L., R. L. Ripperdan, and D. A. Evans (1997), Evidence for a large-scale Early Cambrian reorganization of continental masses by inertial interchange true polar wander, *Science*, *227*, 541–545.

Kustowski, B., G. Ekström, and A. M. Dziewonski (2008), Anisotropic shear-wave velocity structure of the Earth's mantle: A global model, *J. Geophys. Res.*, *113*, B06306, doi:10.1029/2007JB005169.

Li, C., R. D. van der Hilst, E. R. Engdahl, and S. Burdick (2008), A new global model for P wave speed variations in Earth's mantle, *Geochem. Geophys. Geosyst.*, *9*, Q05018, doi:10.1029/2007GC001806.

Liu, L., S. Spasojević, and M. Gurnis (2008), Reconstructing Farallon plate subduction beneath North America back to the late Cretaceous, *Science*, *322*, 934–938.

Maloof, A. C., G. P. Halverson, J. L. Kirschvink, D. P. Schrag, B. P. Weiss, and P. F. Hoffman, (2006), Combined paleomagnetic, isotopic, and stratigraphic evidence for true polar wander from the Neoproterozoic Akademikerbreen Group, Svalbard, *Geol. Soc. Am. Bull.*, *118*, 1099–1124.

Masters, G., G. Laske, H. Bolton, and A. M. Dziewonski (2000), The relative behavior of shear velocity, bulk sound speed, and compressional velocity in the mantle: Implications for chemical and thermal structure, in *Earth's Deep Interior: Mineral Physics and Tomography From the Atomic to the Global Scale*, *Geophys. Monogr. Ser.*, vol. 117, edited by S. Karato et al., pp. 63–87, AGU, Washington, D. C.

Megnin, C., and B. Romanowicz (2000), The 3D shear velocity structure of the mantle from the inversion of body, surface and higher mode waveforms, *Geophys. J. Int.*, *143*, 709–728.

Mitrovica, J. X., and A. M. Forte (2004), A new inference of mantle viscosity based upon joint inversion of convection and glacial isostatic adjustment data, *Earth Planet. Sci. Lett.*, *225*, 177–189.

Montelli, R., G. Nolet, F. A. Dahlen, and G. Masters (2006), A catalogue of deep mantle plumes: New results from finite-frequency tomography, *Geochem. Geophys. Geosyst.*, *7*, Q11007, doi:10.1029/2006GC001248.

Moucha, R., A. M. Forte, J. X. Mitrovica, and A. Daradich (2007), Lateral variations in mantle rheology: Implications for convection related surface observables and inferred viscosity models, *Geophys. J. Int.*, *169*, 113–135.

Mound, J. E., and J. X. Mitrovica (1998), True polar wander as a mechanism for second-order sea-level variations, *Science*, *279*, 534–537.

Müller, R. D., J.-Y. Royer, and L. A. Lawver (1993), Revised plate motions relative to the hotspots from combined Atlantic and Indian Ocean hotspot tracks, *Geology*, *21*, 275–289 (1993).

Müller, R. D., M. Sdrolias, C. Gaina, B. Steinberger, and C. Heine (2008), Long-term sea-level fluctuations driven by ocean basin dynamics, *Science*, *319*, 1357–1362.

Ni, S., E. Tan, M. Gurnis, and D. V. Helmberger (2002), Sharp sides to the African Superplume, *Science*, *296*, 1850–1852.

Panasyuk, S. V., B. H. Hager, and A. M. Forte (1996), Understanding the effects of mantle compressibility on geoid kernels, *Geophys. J. Int.*, *124*, 121–133.

Panning, M. P., and B. A. Romanowicz (2006), A three dimensional radially anisotropic model of shear velocity in the whole mantle, *Geophys. J. Int.*, *167*, 361–379.

Pavoni, N. (1985), Pacific/anti-Pacific bipolarity in the structure of the Earth's mantle, *Eos Trans. AGU*, *66*, 497.

Pavoni, N. (2008), Present true polar wander in the frame of the Geotectonic Reference System, *Swiss J. Geosci.*, *101*, 629–636.

Press, W. H., B. P. Flannery, S. A. Teukolsky, and W. T. Vetterling (1986), *Numerical Recipes: The Art of Scientific Computing*, Cambridge Univ. Press, Cambridge, U. K.

Prévot, M., E. Mattern, P. Camps, and M. Daigniére (2000), Evidence for a 20° tilting of the Earth's rotation axis 110 million years ago, *Earth Planet. Sci. Lett.*, *179*, 517–528.

Ricard, Y., L. Fleitout, and C. Froidevaux (1984), Geoid heights and lithospheric stresses for a dynamic Earth, *Ann. Geophys.*, *2*, 267–286.

Richards, M. A., and B. H. Hager (1984), Geoid anomalies in a dynamic Earth, *J. Geophys. Res.*, *89*, 5987–6002.

Richards, M. A., and B. H. Hager (1989), Effects of lateral viscosity variations on geoid anomalies and topography, *J. Geophys. Res.*, *94*, 10,299–10,313.

Richards, M. A., B. H. Hager, and N. H. Sleep (1988), Dynamically supported geoid highs over hotspots: Observation and theory, *J. Geophys. Res.*, *93*, 7690–7780.

Richards, M. A., Y. Ricard, C. Lithgow-Bertelloni, G. Spada, and R. Sabadini (1997), An explanation for Earth's long-term rotational stability, *Science*, *275*, 372–375.

Ritsema, J., and H. J. van Heijst (2000), Seismic imaging of structural heterogeneity in Earth's mantle: Evidence for large-scale mantle flow, *Sci. Progr.*, *83*, 243–259.

Rouby, H., M. Greff-Lefftz, and J. Besse (2010), Mantle dynamics, geoid, inertia and TPW since 120 Ma, *Earth Planet. Sci. Lett.*, *292*, 301–311.

Sager, W. W., and A. A. P. Koppers (2000), Late Cretaceous polar wander of the Pacific Plate: Evidence of a rapid true polar wander event, *Science*, *287*, 455–459.

Schubert, G., D. L. Turcotte, and P. Olson (2001), *Mantle Convection in the Earth and Planets*, Cambridge Univ. Press, Cambridge, U. K.

Seton, M., C. Gaina, R. D. Müller, and C. Heine (2009), Mid-Cretaceous seafloor spreading pulse: Fact or fiction?, *Geology*, *37*, 687–690.

Simmons, N. A., A. M. Forte, and S. P. Grand (2006), Constraining mantle flow with seismic and geodynamic data: A joint approach, *Earth Planet. Sci. Lett.*, *246*, 109–124.

Simmons, N. A., A. M. Forte, and S. P. Grand (2009), Joint seismic, geodynamic and mineral physical constraints on three-dimensional mantle heterogeneity: Implications for the relative importance of thermal versus compositional heterogeneity, *Geophys. J. Int.*, *177*, 1284–1304.

Steinberger, B. (2007), Effect of latent heat release at phase boundaries on flow in the Earth's mantle, phase boundary topography and dynamic topography at the Earth's surface, *Phys. Earth Planet. Inter.*, *164*, 2–20.

Steinberger, B., and A. Calderwood (2006), Models of large-scale viscous flow in the Earth's mantle with constraints from mineral physics and surface observations, *Geophys. J. Int.*, *167*, 1461–1481.

Steinberger, B., and C. Gaina (2007), Plate tectonic reconstructions predict part of Hawaiian hotspot track to be preserved in Bering Sea, *Geology*, *35*, 407–410.

Steinberger, B., and R. J. O'Connell (1997), Changes of the Earth's rotation axis owing to advection of mantle density heterogeneities, *Nature*, *387*, 169–173.

Steinberger, B., and R. J. O'Connell (2002), The convective mantle flow signal in rates of true polar wander, in *Ice Sheets, Sea Level and the Dynamic Earth*, *Geodyn. Ser.*, vol. 29, edited by J. X. Mitrovica and L. L. A. Vermeersen, pp. 233–356, AGU, Washington, D. C.

Steinberger, B., and T. H. Torsvik (2008), Absolute plate motions and true polar wander in the absence of hotspot tracks, *Nature*, *452*, 620–623.

Steinberger, B., R. Sutherland, and R. J. O'Connell (2004), Prediction of Emperor-Hawaii seamount locations from a revised model of global plate motion and mantle flow, *Nature*, *430*, 167–173.

Su, W.-J., R. L. Woodward, and A. M. Dziewonski (1994), Degree-12 model of shear velocity heterogeneity in the mantle, *J. Geophys. Res.*, *99*, 6945–6980.

Tarduno, J. A. (2007), On the motion of Hawaii and other mantle plumes, *Chem. Geol.*, *241*, 234–247.

Tarduno, J. A., and J. Gee (1995), Large-scale motion between Pacific and Atlantic hotspots, *Nature*, *378*, 477–480.

Tarduno, J. A., and A. V. Smirnov (2001), Stability of the Earth with respect to the spin axis for the last 130 million years, *Earth Planet. Sci. Lett.*, *184*, 549–553.

Thorne, M. S., E. J. Garnero, and S. Grand (2004), Geographic correlation between hot spots and deep mantle lateral shear-wave velocity gradients, *Phys. Earth Planet. Inter.*, *146*, 47–63.

Torsvik, T. H., M. A. Smethurst, K. Burke, and B. Steinberger (2006), Large igneous provinces generated from the margins of the large low-velocity provinces in the deep mantle, *Geophys. J. Int.*, *167*, 1447–1460.

Torsvik, T. H., R. D. Müller, R. Van der Voo, B. Steinberger, and C. Gaina (2008), Global plate motion frames: Toward a unified model, *Rev. Geophys.*, *46*, RG3004, doi:10.1029/2007RG000227.

Torsvik, T. H., B. Steinberger, M. Gurnis, and C. Gaina (2010), Plate tectonics and net lithosphere rotation over the past 150 My, *Earth Planet. Sci. Lett.*, *291*, 106–112, doi:10.1016/j.epsl.2009.12.055.

Tsai, V. C., and D. J. Stevenson (2007), Theoretical constraints on true polar wander, *J. Geophys. Res.*, *112*, B05415, doi:10.1029/2005JB003923.

van der Meer, D. G., W. Spakman, D. J. J. van Hinsbergen, M. L. Amaru, and T. H. Torsvik (2010), Towards absolute plate motions constrained by lower-mantle slab remnants, *Nat. Geosci.*, *3*, 36–40.

van der Voo, R., W. Spakman, and H. Bijwaard (1999a), Mesozoic subducted slabs under Siberia, *Nature*, *397*, 246–249.

van der Voo, R., W. Spakman, and H. Bijwaard (1999b), Tethyan subducted slabs under India, *Earth Planet. Sci. Lett.*, *171*, 7–20.

Wang, Y., and L. Wen (2004), Mapping the geometry and geographic distribution of a very low velocity province at the base of the Earth's mantle, *J. Geophys. Res.*, *109*, B10305, doi:10.1029/2003JB002674.

Wessel, P., and L. W. Kroenke (2008), Pacific absolute plate motion since 145 Ma: An assessment of the fixed hot spot hypothesis, *J. Geophys. Res.*, *113*, B06101, doi:10.1029/2007JB005499.

Wessel, P., and W. H. F. Smith (1998), New, improved version of the Generic Mapping Tools released, *Eos Trans. AGU*, *79*, 579.

Zhang, S., and U. Christensen (1993), Some effects of lateral viscosity variations on geoid and surface velocities induced by density anomalies in the mantle, *Geophys. J. Int.*, *114*, 531–547.

Zhong, S. J., and G. F. Davies (1999), Effects of plate and slab viscosities on geoid, *Earth Planet. Sci. Lett.*, *170*, 487–496.

Zhong, S. J., N. Zhang, Z. X. Li, and J. H. Roberts (2007), Supercontinent cycles, true polar wander, and very long-wavelength mantle convection, *Earth Planet. Sci. Lett.*, *261*, 551–564.